Fragmentation Cross Sections of ^{28}Si at Beam Energies from 290A to 1200A MeV

C. Zeitlin [a,*], A. Fukumura [b], S.B. Guetersloh [a], L.H. Heilbronn [a], Y. Iwata [b], J. Miller [a], T. Murakami [b]

[a] *Lawrence Berkeley National Laboratory, Berkeley, California 94720*
[b] *National Institute of Radiological Sciences, Chiba, Japan*

Abstract

In planning for long-duration spaceflight, it will be important to accurately model the exposure of astronauts to heavy ions in the Galactic Cosmic Rays (GCR). As part of an ongoing effort to improve heavy-ion transport codes that will be used in designing future spacecraft and habitats, fragmentation cross sections of ^{28}Si have been measured using beams with extracted energies from 290A MeV to 1200A MeV, spanning most of the peak region of the energy distribution of silicon ions in the GCR. Results were obtained for six elemental targets: hydrogen, carbon, aluminum, copper, tin, and lead. The charge-changing cross sections are found to be energy-independent within the experimental uncertainties, except for those on the hydrogen target. Cross sections for the heaviest fragments are found to decrease slightly with increasing energy for lighter targets, but increase with energy for tin and lead targets. The cross sections are compared to previous measurements at similar energies, and to predictions of the NUCFRG2 model used by NASA to evaluate radiation exposures in flight. For charge-changing cross sections, reasonable agreement is found between the present experiment and those of Webber *et al.* and Flesch *et al.*, and NUCFRG2 agrees with the data to within 3% in most cases. Fragment cross sections show less agreement between experiments, and there are substantial differences between NUCFRG2 predictions and the data.

Key words: heavy ions, fragmentation, Galactic Cosmic Rays, shielding

1. Introduction

High-energy heavy ions in the Galactic Cosmic Radiation (GCR) are both penetrating and highly ionizing, and therefore pose a health risk to astronauts on long-duration spaceflight [1]. The differential flux (dJ/dE) distributions of these ions [2] have broad peaks between about 300A and 600A MeV, with long high-energy tails extending over several decades. Many energetic GCR ions have ranges well in excess of ten grams per square centimeter in any elemental material, including hydrogen; this is beyond the depth of practical spacecraft shielding. The charged-particle flux impinging on a spacecraft is modified considerably as the incident particles undergo nuclear interactions and ionization energy loss in the walls of the spacecraft, internal equipment racks, etc. The resulting radiation fields in inhabited areas are complex and depend on the distribution of materials in the immediate vicinity. Space radiation environment models [3] as well as transport models [4] are needed to estimate dose and dose equivalent (the present metric of radiation-induced cancer risk) received by astronauts at the skin and internal sites such as the eye, blood-forming organs, and central nervous system. Prior to establishing a human pres-

* 1 Cyclotron Road, MS74R0197, Berkeley, CA, USA 94720, phone: (510)486-5518, fax: (510)486-6949
Email address: cjzeitlin@lbl.gov (C. Zeitlin).

ence in deep space for extended periods of time, it must be shown that model predictions of radiation risk are accurate. As part of an ongoing effort to test and improve NASA's transport models, we have undertaken an extensive series of measurements with heavy ion beams in order to fill gaps in the database of relevant fragmentation cross sections.

Previously, we have reported cross sections for 1.05A GeV ^{56}Fe [5] and 600A MeV ^{20}Ne [6]. Here, we report cross sections for ^{28}Si beams with extracted energies of 290A, 400A, 600A, and 800A MeV. When free-space doses from GCR heavy ions are plotted as a function of atomic number [7], silicon stands out prominently, along with Fe, O, C, and Mg. The contribution of silicon to dose equivalent in free space is second only to that of iron. Further, silicon ions are copiously produced in the fragmentation of Fe and other heavier projectiles. Thus the interaction cross sections of silicon ions are highly relevant to the space radiation problem.

2. Overview of Experiments

Beams of ^{28}Si with extraction energies of 290A, 400A, 600A, and 800A MeV were produced at the Heavy Ion Medical Accelerator in Chiba (HIMAC) at the National Institute of Radiological Sciences. Experiments with these beams were conducted between 1998 and 2006. Data were also obtained with a beam of ^{28}Si at 1200A MeV, at the Brookhaven National Laboratory's Alternating Gradient Synchrotron in 1999.

Using established methods, we present here charge-changing and fragment production cross sections for charges from 6 to 13, on targets ranging from hydrogen [1] to lead.

All measurements were performed using silicon detectors for particle identification, similar to those described in Refs. [5, 6]. The details of the detector configurations varied between experiments, but in all cases the goal was to measure charge-changing and "heavy" (charge $Z \geq 6$) fragment production cross sections using large-acceptance detectors, and to measure light fragment cross sections using small-acceptance detectors. The acceptance angles of the silicon detectors downstream of the target in the different experiments are summarized in Table 1. By acceptance angle, we mean the half-angle of the cone defined by the point at the center of the target and the circumference of the detector's active area. Measured spectra at a particular acceptance depend strongly on beam energy owing to the tendency of forward-going fragments to retain the velocity and direction of the primary.

Figure 1 shows schematic representations of the configurations corresponding to, in the upper drawing, the 1200A MeV experiment at the AGS; in the middle figure, the 2002-4 experiments at 400A, 600A, and 800A MeV; and in the bottom drawing, the 2006 run at 800A MeV. For the 290A MeV run in 2004, the configuration was the same as shown in the middle figure, but with detectors 3mm1 and 3mm2 removed. The configuration for the 1998 run at 600A MeV was shown in Ref. 6. The 1999 HIMAC configuration with a 400A MeV beam resembles the AGS configuration, though without the PSD pair upstream of the target, and with an additional, single 5mm detector placed immediately downstream of the target.

Four detector types were employed: triggers (TR), about 300 μm thick with a 4 mm active radius in the HIMAC experiments and a 1 cm radius in the AGS experiment; Position-Sensitive Detectors (PSDs), roughly 1 mm thick with 2 cm active radii; 3mm detectors with 3 mm depth and 1.1 cm active radii; and 5mm detectors, 5mm thick with about a 2 cm active radii. All detectors are lithium-drifted except the TR's.

Targets of C, CH_2, Al, Cu, Sn, and Pb were used in all experiments. For all beam energies except 290A MeV, we obtained at least two data sets per target material, varying the depths. This method gives a measure of the systematic errors in the analysis, because the cross sections for a given material must be independent of target depth, provided that the cross sections do not depend strongly on small differences in energy.

Before entering the target, beam ions lose energy in a thin window at the end of the vacuum line, in an air gap between the window and the detectors, and in the detectors upstream of the target. Due to the variety of target materials and depths, beam ions at target center had varying energies; e.g., with an extracted energy of 400A MeV, target-center energies were calculated to be between 340 and 364A MeV. Accordingly, in the results below, the energy of this beam is given as (352 $\pm$12)A MeV, and similarly for the other energies. We refer throughout to energies at target center as E_{tc}.

The fraction of primaries interacting in the target was calculated with a simple geometric cross sec-

[1] Hydrogen-target results are obtained with carbon and polyethylene cross sections.

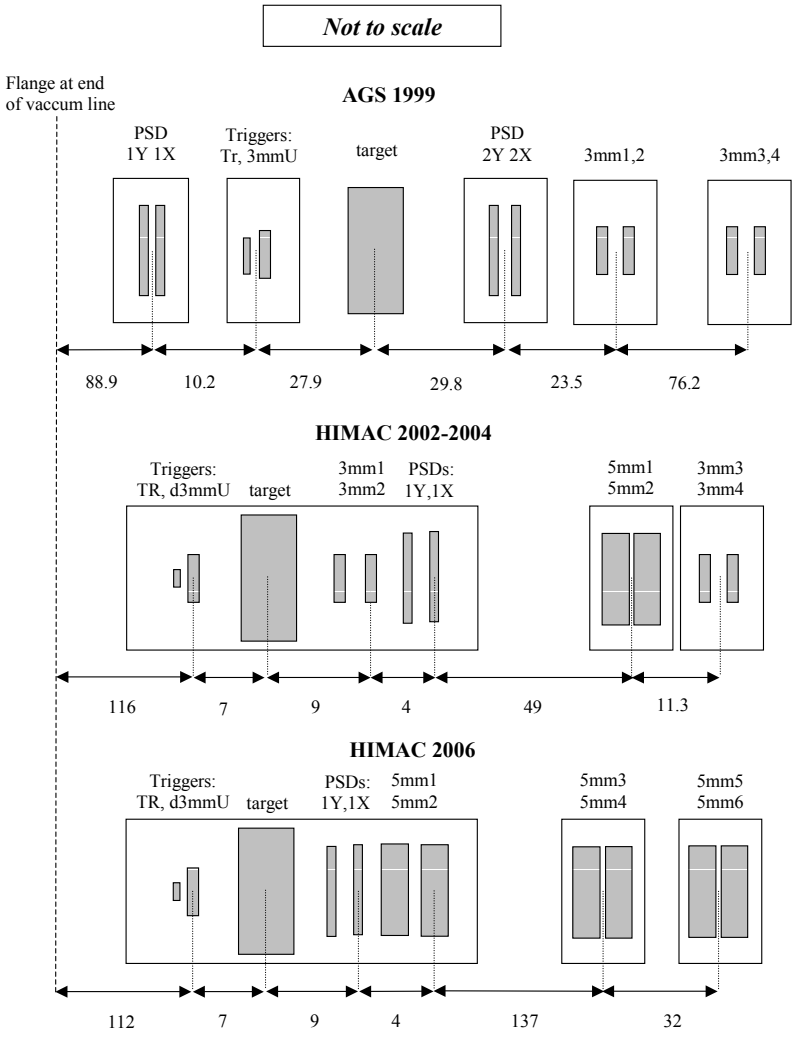

Fig. 1. Schematic drawings, not to scale, for the 1999 AGS runs (upper), for the 2002-2004 HIMAC runs except for the 290A MeV beam (middle), and for the 2006 HIMAC run with the 800A MeV (lower). All distances are in centimeters. Detector types are explained in the text. Each large rectangle surrounding the detectors is meant to represent the holder. Each holder has a mylar window of thickness = 0.001 on both the front and back face for light reduction.

E (A MeV)	600	400	1200	400,600,800	290	800
Year(s)	1998	1999	1999	2002-4	2004	2006
1^{st} Detector Type	3mm	5mm	PSD	3mm	PSD	PSD
θ_{acc}	7.3 °	8.3 °	3.7 °	7.3 °	8.7 °	16 °
2^{nd} Detector Type	PSD	PSD	3mm	PSD	5mm	5mm
θ_{acc}	8.7 °	7.2 °	1.2 °	8.7 °	1.8 °	10.3 °
3^{rd} Detector Type	3mm	3mm	3mm	5mm	3mm	5mm
θ_{acc}	3.9 °	2.6 °	0.5 °	1.8 °	0.9 °	0.7 °
4^{th} Detector Type	3mm	3mm		3mm		
θ_{acc}	2.6 °	1.2 °		0.9 °		

Table 1. Detectors used in the various experiments and their angular acceptances. Detector dimensions are given in the text. The numbering scheme (1^{st}, 2^{nd}, etc.) refers to the order of the detectors on the beamline, with the first detector being closest to the target. All data except those at 1200A MeV were obtained at the HIMAC accelerator.

tion model [8], with results ranging from 0.21 for the thickest carbon target to 0.026 for the thinnest Pb target. As the probability of a primary interaction increases, so do the probabilities for secondary and higher-order interactions, with corresponding increases in the (weakly model-dependent) corrections needed to account for them. On the other hand, when thin targets are used and the fraction of interacting primaries is small, the peaks for fragments one charge unit below the primary (Al for Si beams) can be difficult to distinguish from the low-end tail of the primary peak [2], leading to significant uncertainties in the cross sections. This is particularly true in the lower-energy data sets, where the need to avoid excessive energy loss dictated the use of relatively thin targets. In addition to the overlap of Al and Si distributions, in all of the 290A MeV data and in some runs at higher energies, the C and N fragment peaks are not well-resolved at large acceptance, for reasons explained below.

2.1. *Detector Acceptance*

Acceptance efficiencies were calculated using a simple model that combines fragment angular distributions [9], [10] with the effects of Coulomb multiple scattering in the target. For low-Z targets such as carbon and aluminum, multiple scattering is negligible at these energies, even in fairly thick targets, and the widths of the angular distributions are dominated by the reaction dynamics. For high-Z targets, particularly when the depth is relatively large, Coulomb scattering can dominate the angular distributions. The fraction of fragments within a given angular acceptance decreases as fragment charge and mass decrease. For fragment charges Z > 7, the detectors with the largest acceptances in all cases contain in excess of 99% of the expected angular distributions. This is also true for charges 6 and 7 with a small number of exceptions. The fact that no corrections are needed above charge 7 is due to the strong forward-peaking of the fragment angular distributions and the placement of large-acceptance detectors close to the target exit. [3] Acceptances and background corrections are discussed in more detail below.

The full acceptance of the most-upstream detectors for charge 8 and above can be illustrated with a simple example. We consider the worst case among the data sets analyzed here, the data taken with the 400A MeV beam and a fairly thick copper target of areal density ρx of 5.5 g cm^{-2}. For fragments of charge 8 and mass 16, the width of the angular distribution due to nuclear effects is assumed to be Gaussian and (using equations 3 and 6 of Ref. 9) is expected to have a standard deviation σ_{nuc} of about

[2] The ability to separate primary silicon from aluminum depends on how well individual silicon detectors performed in a given experiment. Performance was seen to vary significantly over time. The event rate during data-taking can also play a role, owing to the effects of overlapping pulses if pole-zero cancellation is not perfect.

[3] In the Goldhaber model of momentum transfer, the parameter σ_0 controls the widths of the fragment momentum distributions, most importantly the transverse components. The parameter is loosely constrained by experimental data and theoretical considerations to be on the order of 100 MeV/c, which is small compared to the longitudinal momenta of the fragments.

1.9 $^\circ$. The Gaussian width of the Coulomb scattering distribution is about 0.5 $^\circ$. The two contributions are added in quadrature to obtain a total width of 2.0 $^\circ$. (This sum is dominated by the nuclear term, which is usually the case for the experiments described here.) The detector with the largest acceptance in this experiment was the PSD1 pair, which subtended a cone of half-angle 6.7 $^\circ$ centered on the beam axis. The acceptance cone therefore contains the angular distribution out to about 3.3 standard deviations, with an integral corresponding to greater than 99.9% of the entire distribution. At higher energies, the longitudinal momentum is greater than in this example, and even more of the fragments would be contained within this (or similarly large) acceptance angle.

3. Cross Sections and Uncertainties

3.1. *Event Selection*

Histograms of ΔE in the detectors upstream of the target position were used to select clean samples in which all events have a single, clearly-identified silicon ion incident on the target. All further cuts are based on correlation of ΔE in pairs of detectors downstream of the target position. These cuts are used to define well-measured events with fragments and surviving primaries; see [5] and [6] for details. One new selection criterion, described below, has been added in this analysis as compared to earlier work.

Detectors downstream of the target are placed in pairs along the beamline so that a correlation plot for each pair can be made. This allows us to remove artifacts that are inevitably present in single-detector spectra. In the analysis of any given detector pair, a cut is made in the correlation plot to require mutually consistent ΔE in the two detectors. This cut removes events in which a nuclear interaction occurred in either detector, or in which one detector or the other gave a spurious reading. When the detector pair being analyzed is not the most-upstream pair, an additional cut is made to remove events in which a primary that survived the target underwent a charge-changing interaction in the detector stack. (Such events are easily identified using the most-upstream detectors, as in Fig. 5 of Ref. [6].) In the present analysis, an additional cut was found to be necessary in the analysis of data in the most-upstream detector pair. This was a cut in the scatter plot of ΔE in the second detector of the most-upstream pair vs. the ΔE in the first detector of the next pair. Figure 2 shows an example, using the 800A MeV beam data from 2004. In a small number of events, indicated by the rectangle, the more-downstream detector (PSD1Y in this example, plotted on the vertical axis) registered a signal consistent with a primary silicon ion, but the more-upstream detector pair (3mm1 and 3mm2) both recorded signals consistent with that of an aluminum fragment. These events must actually have been caused by a silicon ion that survived the target, but was mis-measured in each of the detectors of the most-upstream pair. Though small in number, these events have the undesirable dual effects of causing both the charge-changing and Al production cross sections to appear larger than they actually are. The effect is most pronounced when the target presents a small fraction of an interaction length and the fraction of surviving silicon ions is very high (the fraction can be in excess of 97% in these data). As this effect also depended on detector performance, it varied between data sets; in some data, there were no, or a very small number of, events of this type to be removed, and the cut was unnecessary.

3.2. *Effective Charge Histograms*

Once a sample of well-measured events has been arrived at, the Z_{eff} histogram is generated, as shown in Fig. 3. In Fig. 3(a), we show a histogram of ΔE for clean events in the 3mm1/3mm2 detector pair. (The data are from the 2002 experiment with the 600A MeV extracted beam at HIMAC, incident on a carbon target of 1.31 g cm^{-2} areal density.) Obvious peaks can be seen for the primary species (Z = 14) and several fragment species. As in [5], we define the effective detected charge Z_{eff} as proportional to$\sqrt{\Delta E}$, and fit a Gaussian to the spectrum of surviving primaries to find the value of ΔE at the peak. This value determines a scale factor so that the primary peak can be centered on the primary Z. The factor is used to generate a Z_{eff} histogram, which implicitly assumes that fragments are at or near beam velocity.

Using the Z_{eff} histogram, events are counted by species and the totals entered into a spreadsheet. Corrections as a function of species are applied in the spreadsheet to compensate for events lost due

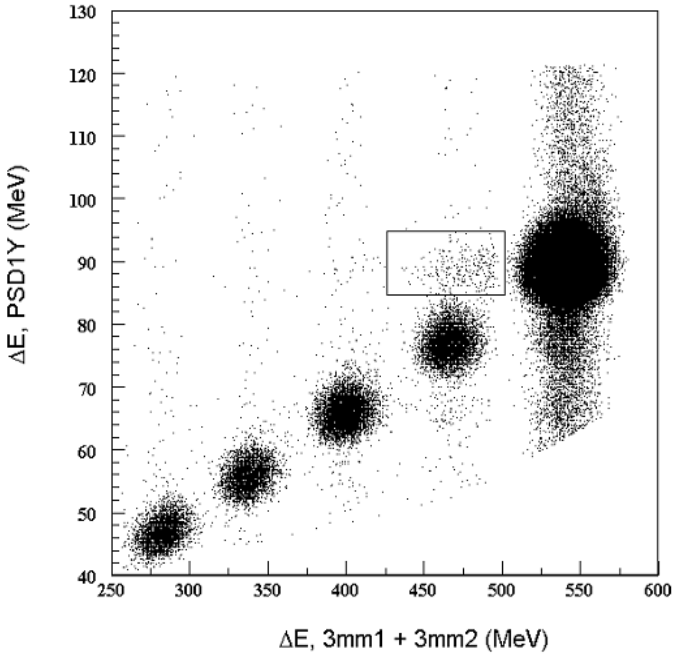

Fig. 2. Scatterplot of deposited energy in a detector downstream of the first detector pair (PSD1Y, vertical axis) vs. deposited energy in the most-upstream detector pair (3mm1 + 3mm2, horizontal axis). The outlined region contains events that would be misidentified as fragments in the 3mm1/3mm2 pair; these events have been removed in the analysis.

to nuclear interactions in the silicon stack.[4] Target-out data are used to correct for changes in the spectra due to interactions in the air gaps, detector dead layer, etc.; and Monte Carlo calculations [11] are used to correct for the effects of secondary and higher-generation interactions in the target. Model-related uncertainties in the latter are estimated to contribute 1 to 2% relative errors to fragment cross sections, which are determined by species (not by isotope). When fragment peaks are clearly separated, counting by species is straightforward, and the uncertainties due to the events in the valleys are very small. However, in some cases, the valleys are only slightly lower than the peaks, and there can be a considerable degree of arbitrariness associated with charge assignments.[5] These ambiguities in identification are most significant for charges 6 to 8, and are discussed in more detail below.

Large acceptance detectors commonly record more than one fragment in an event; such events have Z_{eff} shifted to larger-than-integer values, according to $Z_{eff} = \left(\sum_i Z_i^2\right)^{1/2}$ where the sum runs over all particles within the acceptance. When the leading fragment is near the beam charge, its charge dominates and Z_{eff} is close to an integer. As the charge of the leading fragment decreases, the multiplicity of lighter fragments increases, as does their influence on Z_{eff}. The peaks shift to higher-than-integer values and become less distinct, disappearing altogether below charge 6.[6] In Fig. 3(b), we show the result of the scaling method applied to the same event sample used to make Fig. 3(a). The shift of fragment peaks to above-integer values is pronounced and, as expected, increases as the charge of the leading fragment decreases; for instance, the nominal charge 7 peak is centered near Z = 7.5. At smaller acceptances, the fragment peaks are much closer to integer values.

[4] For each species we use the mass number of the most abundant naturally occurring isotope.

[5] Using histograms scaled to Z has an advantage in the cases where the peaks are not sharp, since we can sum over equal numbers of bins per fragment species. This reduces the degree of subjectivity.

[6] This is due to the many possible combinations of fragments that populate the charge histogram below about half the beam charge at large acceptance, in this and similar experiments.

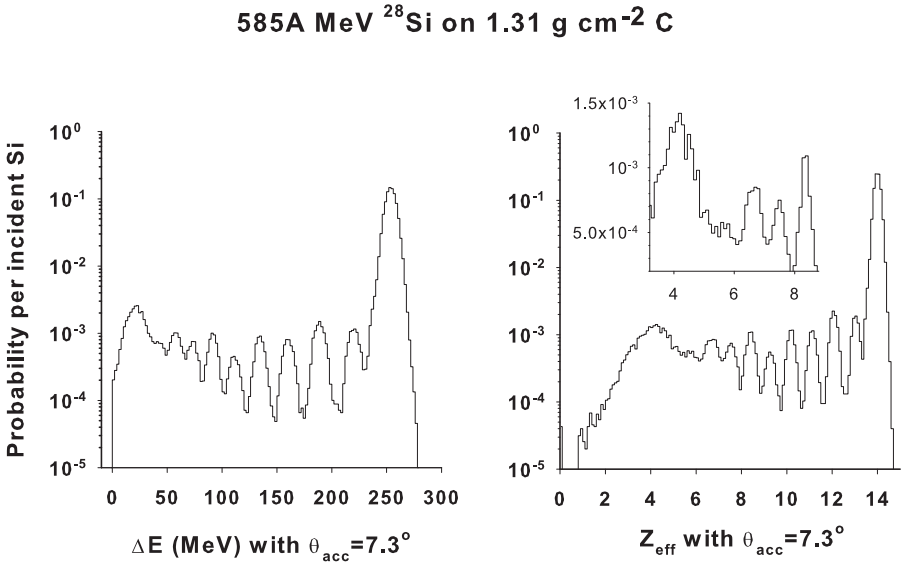

Fig. 3. Deposited energy (left) and Z_{eff} spectra (right) obtained with the 600A MeV ^{28}Si beam at HIMAC incident on a carbon target of 1.31 g cm^{-2} depth. In both plots, the data have been normalized to the probability of observing a given ΔE or Z_{eff} per incident beam ion. The inset figure on the right shows the same data as the larger figure but plotted on a linear scale on the y-axis, for fragments of charge 8 and lower.

3.3. *Error analysis*

When two or more data sets with a given beam energy and target material are available, we average the corrected results to obtain a single set of charge-changing and fragment production cross sections. We have multiple measurements for all beam energy/target material combinations, except for the 290A MeV data.

Based on the experience gained in analyzing many data sets, we assign to each individual measurement an error of 0.003 in the fraction of surviving primary ions. (This is a slight departure from the error assignments made in our previously-published data.) This error propagates into σ_{cc} in a slightly non-trivial way. The result is that the relative error in the cross section is dependent on the fraction of surviving primaries. This method directly takes into account the ambiguities associated with the graphical cuts in both target-in and target-out data that directly affect the surviving-primary fractions; the fractions are related to the cross sections logarithmically. Assigning the error to the surviving primary fraction, and not to the cross section itself as in previous work, means that a measurement with a very thin target, e.g. one that represents 3% of an interaction length to the primary, yields a measurement of σ_{cc} that is good to only 10%. On the other hand, for our thickest targets, the relative error in σ_{cc} is about 1.5%. When we combine data for a given beam energy and target material, these uncertainties are subject to being adjusted upward, as will be described.

The final charge-changing cross section result

for a given beam energy and target material is the weighted average of the individual measurements, where the uncertainty in each is taken to be the quadrature sum of the negligible statistical errors and the systematic errors described above. The systematic errors are applied to all the data sets being combined into the weighted average, and a χ^2 for combining the data sets is calculated. If χ^2 is greater than 1 per degree of freedom (the number of data sets minus one), then the errors for all data sets are simultaneously increased by adding, in quadrature, another contribution to the systematic error. This additional error can be attributed to uncertainties in, e.g., target areal densities or slight differences in the analysis methodology as applied to data sets from different experiments. The upward adjustment of uncertainties proceeds in steps of 0.1% relative error, until we obtain a χ^2 of 1.0 or less per DOF. In most cases, the systematic errors propagated from the 0.003 surviving primary uncertainty are considerably larger than the observed spread of the cross sections, and no upward adjustment is required. Even in these cases, we retain the propagated error in the surviving primary fraction as the minimum uncertainty, as we do not wish to overstate the precision of these measurements. We believe that the spread of the cross section results obtained from similar data sets is more a measure of the consistency with which the analysis methods have been applied than it is a measure of the absolute accuracy of the results.

The uncertainties in the σ_{cc} propagate into those associated with the fragment production cross sections, σ_Z, so the relative error on any single fragment cross section must be at least as large as that on the corresponding σ_{cc}. Additional sources contribute to the uncertainties in the σ_Z: the corrections for secondary and higher-order interactions in the target, particle identification ambiguities, acceptance corrections, etc. These are estimated to add a minimum of 3% uncertainty in quadrature with the statistical errors and the propagated uncertainty from σ_{cc}. When two or more data sets are combined, the systematic error can be adjusted upward as needed. We apply one adjustable error to fragments with Z from 9 to 13, and a separate one to fragments with Z from 6 to 8. Again, a total χ^2 is computed for each group, starting with the adjustable uncertainties set to 0. If necessary, the adjustable systematic errors are increased until χ^2 is less than or equal to the number of degrees of freedom. In practice, the adjustable errors are typically left at 0, with a few cases going up to about 5%. The combined fragment cross sections and uncertainties are given by the weighted averages of the individual data sets.

The relative uncertainties for hydrogen targets, both for fragment and charge- changing cross sections, are larger than for others. This is due both to the propagation of errors from two measurements (C and CH_2), and also because this method requires subtracting one relatively large number from another to obtain a comparatively small number.

3.4. *Species Identification for Charges 6 to 8*

Our method of identifying the leading fragment according to the effective detected charge is susceptible to errors when the effective charge distribution for a given species is not cleanly separated from those of its neighbors. In all the data presented here, clean peaks are invariably seen for charges 9 and above, and the identification of these fragment species is simple. However, obtaining accurate identification of fragment charges 6 to 8 is complicated by four effects: detector acceptance, detector resolution, fragment multiplicity, and the widths of fragment velocity distributions. Each of these effects grows in importance as fragment charge decreases. For large-acceptance detectors, the broadening of velocity distributions is combined with the presence, on most but not all events, of one or more non-leading fragments, resulting in further broadening of ΔE and Z_{eff} distributions. Detector resolution plays a role: generally, thicker detectors have better resolution due to better charge-collection statistics. However, in some of the experiments reported here, PSDs (about 1 mm thickness) were used as the large-acceptance detectors, and their resolution is generally not as good as that obtained with 3mm or 5mm thick detectors.

There are two main contributors to the width of fragment velocity distributions, longitudinal momentum transfer in the interaction, and variations in energy loss in the target. The latter depend on the exact location of the charge-changing interaction. Both effects grow in significance as the charge of the leading fragment decreases. For a given fragment charge, an interaction near the target entrance will, on average, yield a higher-velocity fragment than an interaction near the target exit. This effect is more pronounced at low beam energies than at higher energies, and becomes more significant as target depth increases. The overlap of the effective charge dis-

tributions is further exacerbated in the charge 6 to 8 range by non-leading fragments, particularly helium, which is copiously produced. For example, a nitrogen fragment can be accompanied by up to three helium ions; assuming all fragments are at beam velocity, the combination produces a Z_{eff} of 7.8, close to the nominal oxygen peak. At the other extreme, a single nitrogen ion, produced near the entrance of a high-Z target, exits with a velocity slightly higher than that of the beam ions and is recorded as having Z_{eff} of 6.8 (calculated by scaling to the primary, as in the data analysis). Thus events with a leading nitrogen fragment can span an entire unit in the effective charge plot; events with carbon fragments can span slightly more than one charge unit. This explains the lack of valleys in the charge 6 to 8 regions of many of the large-acceptance histograms.

In the charge histogram shown in Fig. 3b, we show an inset figure with the same data on a linear scale, for charges 8 and below. It appears the continuum below charge 6 may be "feeding up" into the higher-charge peaks due to the effects mentioned above. A more insidious, related problem is that the charge 6 distribution may feed into charge 7, charge 7 into charge 8, etc. The complexity is illustrated in Fig. 4, which shows the detected charge in a small-acceptance detector (on the ordinate) against detected charge in a large-acceptance detector (abcissa) for charges 5 to 10, using data obtained with the 800A MeV beam. Dashed lines forming a rectangular grid have been drawn on the figure to indicate, approximately, the ranges in the charge histograms that would be used to count fragments by species for charges 6 through 8. [7]

In Figure 4, it can be seen that for charge 10 (and for the higher charges not shown), there appears to be essentially no contamination from lower charges. The situation for charges 6 to 8, however, is less clear, and it is evident that correct identification of Z is easier in the downstream detectors. For instance, consider the events that are clearly identified as Z = 6 in the downstream detectors; a substantial number are identified as charge 7 in the upstream detectors, and some would be grouped in the category of events with Z < 6. The losses are partly (perhaps fully) compensated by feeding-up of events with a lower-charge leading fragment and some misidentification of Z = 7 as Z = 6. Given these difficulties, it seems clear that the downstream detectors are more reliable for charge identification of the leading fragment in this range of charges, with the disadvantage that the limited acceptances require model-dependent corrections.

To the extent that neighboring fragments have similar production cross sections, the overlapping of the charge distributions at large acceptance may have little net effect on the cross sections, provided the number of particles misidentified in one direction (e.g., actual Z = 7, identified as Z = 8) is compensated by a roughly equal number of particles misidentified in the other direction (e.g., Z = 8 identified as Z = 7). However, when the misidentification is asymmetrical, which would be the case if the production cross sections vary substantially from one species to the next, the fragment cross section results may be significantly affected.

The apparent loss of resolution for charges 6 to 8 is due in part to energy-dependent effects. The 290A MeV and 400A MeV data are the most problematic in this regard, but even the data at higher energies lacked clear separation between charges 6 and 7 in some cases. For all energies, the spectra obtained in detectors with small acceptance are easier to interpret because the non-leading fragments tend to be outside the acceptance. These spectra show clear separation between neighboring peaks, and no suggestion of a "feed-up" effect. Peaks for charges below 6 (and certain combinations of light fragments) can also be seen. However, because of the small acceptance, some leading fragments are also outside the acceptance, necessitating model-dependent corrections. Thus, with these data, we can extract cross sections from large-acceptance data that may be inaccurate due to charge identification errors, and we can extract cross sections from small-acceptance data that must be corrected. We have performed a careful comparison of the results obtained by the two methods using 400A, 600A, and 800A MeV data, and find that the two methods are mutually consistent to better than 7% on average, as explained in detail below.

To obtain cross sections for charges 6 to 8 using the small-acceptance measurements, we must first determine the charge-changing cross sections in detector pairs placed relatively far from the target. Event selections were made as per the methods described above. An additional correction is made, if needed, to bring the charge-changing cross section

[7] Events in which a charge-changing interaction occurred in the detector stack have for the most part been removed in this plot by requiring that Z in the downstream detectors is within one charge unit of Z in the upstream detectors. This requirement was imposed in order to simplify the plot, but it is not applied in the analysis.

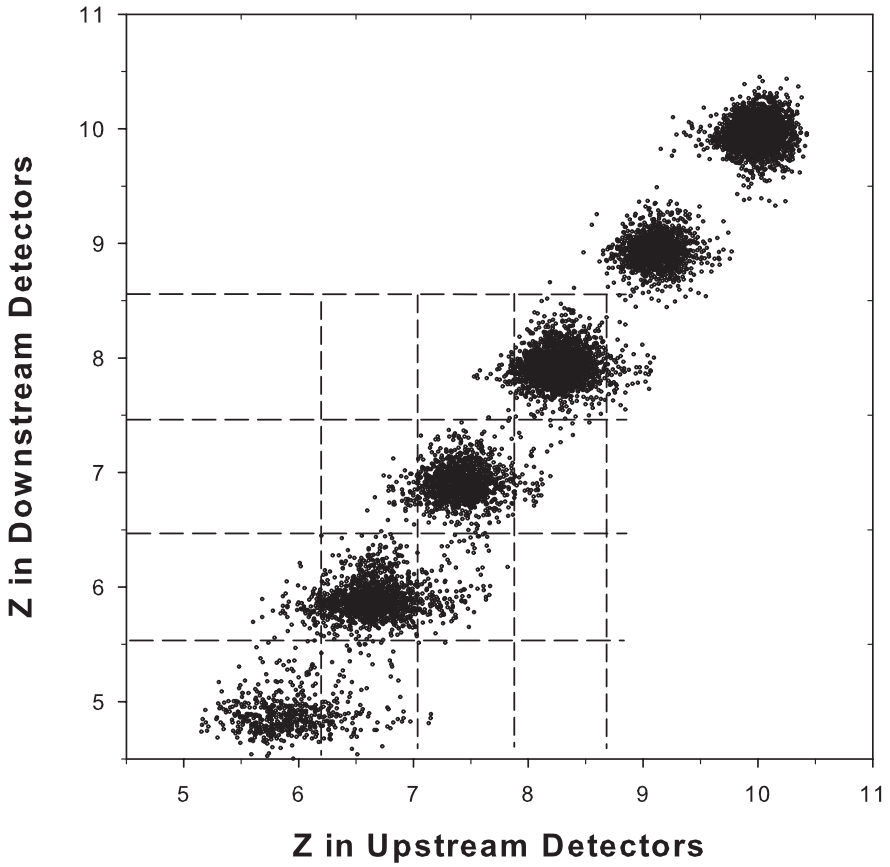

Fig. 4. Fragment charge as measured by a small-acceptance detector plotted against charge as measured in a large-acceptance detector. The boxes indicate, approximately, the regions that would be associated with a particular charge in the charge histograms, which are projections of these data onto one axis or the other. Of particular concern are the events outside the boxes, most prominently seen for charges 6 and 7.

at small acceptance into agreement with that measured in the same run at large acceptance. (This ad hoc correction accounts for primaries lost due to scattering out of the smaller acceptance, and those lost by the cut criteria that are by necessity more stringent for primaries than for fragments.) With the charge-changing cross section determined, the fragment cross sections are calculated in the usual way. Acceptance corrections as calculated using the model described in Section 2.1 were applied to account for both nuclear and Coulomb effects. Corrections were applied to all fragment cross sections as measured in the small-acceptance detectors, though they are typically negligible above charge 8. For each data run, the σ_0 parameter in the Goldhaber model was treated as a free parameter and was adjusted until the cross sections for fragment charges 9 through 12 measured at small acceptance were brought into best agreement (determined by minimizing the total χ^2) with those obtained at large acceptance. The cross sections for charges 6 to 8 were computed using this same value of σ_0.

The results of the two methods for obtaining charge 6 to 8 fragment cross sections are plotted against one another in Fig. 5, with the symbols chosen to differentiate between 400A, 600A, and 800A MeV data. If there were a systematic problem with misidentification of fragments in the large-acceptance cross sections, we would have expected predominantly smaller cross sections in the corrected small-acceptance results. However, as can be seen in Fig. 5, no consistent trend is seen. A more quantitative assessment was made by histogramming the ratios of the cross sections and fitting the resulting distribution with a Gaussian; the fit yields a central value of 0.99, with a standard deviation

of 0.063. Accordingly, we (conservatively) assign an additional 6.5% uncertainty to the cross sections for charge 6, 7, and 8 fragments, added in quadrature with all the other uncertainties.

4. Charge-Changing Cross Sections

4.1. *Energy dependence*

Results for the charge-changing cross sections, σ_{cc}, are shown in Table 2 for all energies and targets. The E_{tc} ranges are shown in parentheses in the first column; the central value is the average over all runs, and the quoted errors cover the entire spread of target-center energies.

We searched for energy dependence in the σ_{cc} results by computing χ^2 for the null hypothesis of energy independence across the range measured here. The computed values are shown in the next-to-last row of Table 2. Except for hydrogen, the charge-changing cross sections are consistent with energy independence. No statistically significant trends are seen, regardless of target mass, for carbon and heavier targets. The hydrogen-target cross sections are not consistent with energy independence, and show an increase in σ_{cc} in the higher-energy data. This is qualitatively consistent with the trend seen in the Webber *et al.* experiments, but the magnitude of the effect is only slightly beyond the estimated uncertainties in our data.

4.2. *Comparison with other measurements*

In Table 2 we show cross sections from Flesch *et al.* at about 450A MeV [12], using CR-39 and most of the same target materials, and from Webber *et al.* [13] at 503A, 770A, and 1296A MeV target-center energies, using H and C targets only. To compare the deviations between experiments, we computed for each target the standard deviations between any two measurements at comparable energies. The standard deviations were then averaged over targets, so when we compare the present data to those of Flesch *et al.*, targets include H, C, Al, Cu, and Pb; and when we compare to Webber *et al.*, targets are H and C only. The results are shown in Table 3. With the exception of the highest energy data (where only two σ_{cc} are compared), the average level of agreement is in the range from 2.3% to 3.9%. This is again comparable to, though slightly larger than, the claimed uncertainties in the experiments.

In summary, for all targets except hydrogen, the charge-changing cross sections from the present experiment show no discernible energy dependence over the 270A to 1150A MeV range. The hydrogen-target cross section increases slightly with energy. RMS differences of our data when compared to previously-reported cross sections are under 5% in all cases but two[8] and are typically in the 2% to 3% range.

4.3. *Comparison to NUCFRG2 model predictions*

Calculated values from the NUCFRG2 model [14] are shown in each section of Table 2. The calculated cross sections increase slightly with energy, whereas the data are consistent with energy independence for targets other than H. However, the predicted energy dependence is slight, on the same order as the experimental uncertainties. Therefore we cannot exclude the possibility that the predicted dependence is correct, and simply too small an effect for us to measure. The energy dependence of the H-target data is reproduced fairly well. In Table 3, we show the standard deviations between NUCFRG2 and our data, divided by the measured cross section, averaged over all targets at a given beam energy. The largest average discrepancy is 3.7% for the 290A MeV beam, with the measured cross sections being larger than predicted; at all higher energies, the agreement is better, typically around 2%.

5. Fragment Cross Sections for Charges 6 to 13

5.1. *Results*

Tables 4 to 9 show cross sections for the production of fragments with charges 6 through 13 in the various target materials, ordered by increasing mass number of the target material. Some features of the data are obvious and are expected – e.g., for a given beam energy and fragment species, the σ_Z grow monotonically as target mass increases. Another prominent feature is the suppression of F production compared to Ne and O, which is seen with all target materials. Cross sections for C and O are

[8] The two cases are for carbon targets at 1150A MeV when compared with Webber *et al.* at 1296A MeV, and for hydrogen targets at 765A MeV when compared with Webber *et al.* at 770A MeV.

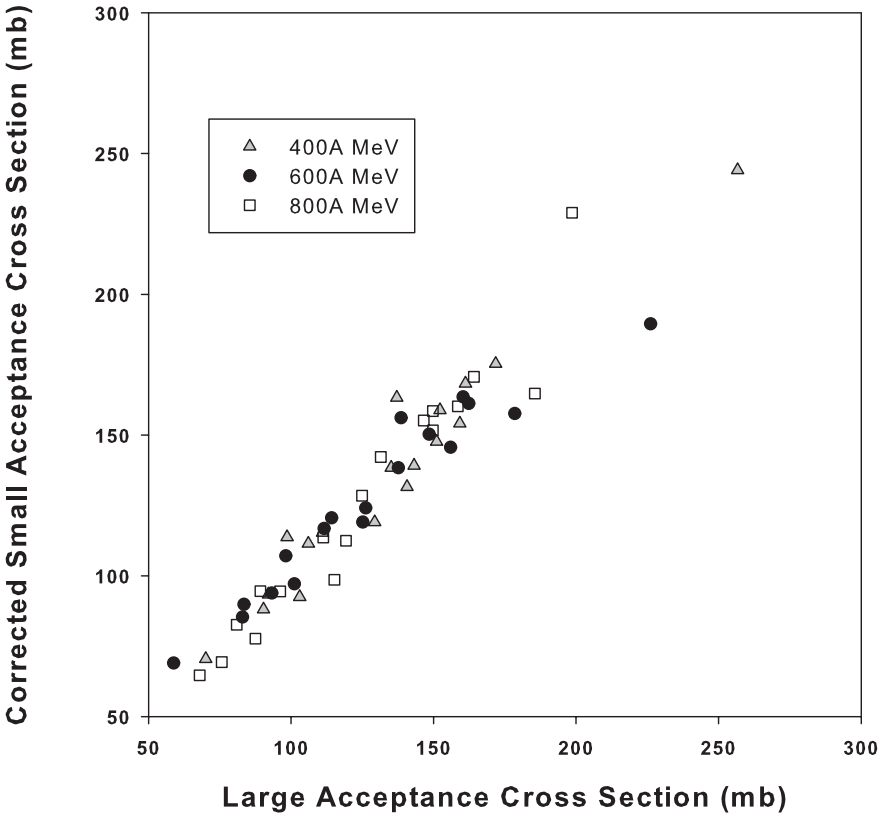

Fig. 5. Correlation plot of cross sections obtained with large-acceptance detectors (horizontal axis) and small-acceptance detectors (vertical axis). The small-acceptance results have been corrected for missing fragments according to the model described in Sec. 2.1. The differences between the two methods contribute an additional 6.5% to our systematic uncertainties.

typically within 10-15% of each other, and are about double the F cross sections. Cross sections for Al (Z = 13) production are smaller than those for Mg (Z = 12) for H, C, and Al targets. As target mass increases, electromagnetic dissociation [15] accounts for a significant portion of the single-charge removal cross section, which may explain the observation that the Al production cross sections are larger than those for Mg production for the Cu, Sn, and Pb targets. Figure 6 shows, for the 600A MeV and 1200A MeV data, the σ_Z as a function of ΔZ for C, Al, Cu, and Pb targets for charges 6 to 13, in each case divided by the corresponding charge-changing cross section σ_{cc}. The data for other beam energies look very similar when plotted this way. The hydrogen results stand well apart from those for the other targets. With few exceptions, which we discuss below, the line segments that connect the data points for C and heavier targets are nearly parallel to one another and do not cross. This suggests that the σ_Z/σ_{cc} ratios for these targets, and in this range of ΔZ, could be parameterized with a form having weak dependence on the target.

At 600A MeV, the only instance of lines crossing for the C and heavier targets is where the Pb target, ΔZ = 1 point rises above the point for Sn; this is presumably due to a large contribution from electromagnetic dissociation with this very high-Z target. At 1200A MeV, the effect of electromagnetic dissociation appears to be more significant, as the ΔZ = 1 point is relatively high for both Pb and Sn, and the ΔZ = 2 point is high for Pb. In general, in the 1200A MeV data, the lines for C and heavier targets are more compressed than in the 600A MeV data. We note that the ΔZ = 8 (charge 6 production) cross section for the hydrogen target rises by nearly a factor of 2 from 290A MeV to 800A and 1200A MeV.

Table 2. Charge-changing cross sections compared to other experiments and to NUCFRG2.

	E_{tc}**(A MeV)**	**H**	**C**	**Al**	**Cu**	**Sn**	**Pb**
This work	262 to 278	393 ± 27	1131 ± 34	1573 ± 76	2267 ± 185	3076 ± 280	3808 ± 466
Nucfrg2	270	364	1112	1508	2138	2806	3629
This work	340 to 364	371 ± 12	1125 ± 16	1528 ± 37	2219 ± 145	2991 ± 145	3779 ± 261
Flesch *et al.*	455	368 ± 17	1136 ± 13	1638 ± 23	2201 ± 29		3751 ± 63
Nucfrg2	352	386	1115	1511	2185	2815	3646
This work	536 to 568	393 ± 12	1142 ± 16	1547 ± 45	2281 ± 41	2937 ± 89	3848 ± 87
Webber *et al.*	503	379 ± 9	1176 ± 12				
Nucfrg2	550	413	1154	1554	2198	2884	3728
This work	760 to 770	424 ± 12	1110 ± 14	1546 ± 27	2232 ± 92	2849 ± 74	3758 ± 103
Webber *et al.*	770	387 ± 10	1183 ± 12				
Nucfrg2	765	426	1196	1603	2257	2956	3832
This work	1136 to 1158	426 ± 15	1100 ± 16	1546 ± 41	2298 ± 44	3067 ± 91	3930 ± 94
Webber *et al.*	1296	407 ± 10	1215 ± 12				
Nucfrg2	1150	432	1208	1614	2301	3017	3925
Avg. σ_{cc}		401 ± 6	1119 ± 8	1544 ± 17	2271 ± 25	2947 ± 45	3847 ± 54
χ^2 en.-indep.	(4 d.o.f.)	13.1	4.0	0.3	1.5	4.1	1.6

Data Set 1	E_{tc}(A MeV)	Data Set 2	E_{tc}(A MeV)	(st.dev./av. σ_{cc})
This work	352 ± 12	Flesch *et al.*	455	1.5%
This work	552 ± 16	Flesch *et al.*	455	2.7%
Flesch *et al.*	455	Webber *et al.*	503	2.3%
This work	552 ± 16	Webber *et al.*	503	2.3%
This work	765 ± 5	Webber *et al.*	770	5.5%
This work	1147 ± 11	Webber *et al.*	1296	5.1%
This work	270 ± 8	NUCFRG2	270	3.7%
This work	352 ± 12	NUCFRG2	350	2.0%
This work	552 ± 16	NUCFRG2	550	1.8%
This work	765 ± 5	NUCFRG2	765	2.2%
This work	1147 ± 11	NUCFRG2	1150	2.1%

Table 3. The top six rows show the relative agreement of charge-changing cross section measurements by different groups. The last five rows show the average agreement of the present data with the NUCFRG2 model predictions.

5.2. *Energy dependence*

The fragment production cross sections shown in Tables 4-9 are difficult to characterize in a general way. To help visualize the trends, in Fig. 7 we plot, for each target material, the fragment cross section at a particular energy (for the 400A MeV and higher energy beams), divided by the cross section for that fragment species measured at 290A MeV. Each fragment species is represented by a different color, and lines have been drawn between data points to guide the eye. For the moment, we focus on C and heavier targets; we will discuss the hydrogen-target results separately. In the C and Al target data, a strong trend is seen in which the fragment cross sections decrease as energy increases. For Cu, there appears to be little or no energy dependence; for Sn and Pb, matters are more complicated. In the large majority of cases, the ratios are less than 1, indicating that the $Z_f \geq 6$ cross sections are larger at

Table 4. Fragment production cross sections of silicon on hydrogen.

Si + H	This work	This work	Flesch *et al.*	Webber *et al.*	This work	This work	Webber *et al.*	This work	Webber *et al.*
E_{beam}	263	350	467	503	560	765	770	1147	1296
σ(Z=13)	86 ± 7	79 ± 4	65 ± 6	87 ± 4	73 ± 3	75 ± 3	83 ± 4	66 ± 4	78 ± 4
σ(Z=12)	104 ± 8	96 ± 5	79 ± 7	84 ± 4	86 ± 3	83 ± 3	76 ± 4	71 ± 4	75 ± 4
σ(Z=11)	53 ± 5	47 ± 3	41 ± 5	37 ± 2	45 ± 2	46 ± 2	37 ± 2	41 ± 2	38 ± 2
σ(Z=10)	48 ± 5	44 ± 3	35 ± 5	36 ± 2	48 ± 2	47 ± 2	36 ± 2	41 ± 2	39 ± 2
σ(Z=9)	16 ± 2	18 ± 1	12 ± 3	16 ± 2	21 ± 1	22 ± 1	16 ± 2	21 ± 2	18 ± 2
σ(Z=8)	36 ± 7	32 ± 5	25 ± 4	36 ± 2	38 ± 4	42 ± 5	35 ± 2	43 ± 6	36 ± 2
σ(Z=7)	22 ± 5	15 ± 4	16 ± 4	16 ± 2	25 ± 3	27 ± 4	18 ± 2	31 ± 5	20 ± 2
σ(Z=6)	18 ± 6	18 ± 5	33 ± 5	23 ± 2	27 ± 5	34 ± 5	25 ± 2	34 ± 7	32 ± 3

Table 5. Fragment production cross sections of silicon on carbon.

Si + C	This work	This work	Flesch *et al.*	Webber *et al.*	This work	This work	Webber *et al.*	This work	Webber *et al.*
E_{beam}	266	344	467	503	560	765	770	1147	1296
σ(Z=13)	140 ± 7	122 ± 4	125 ± 5	130 ± 2	118 ± 3	113 ± 3	157 ± 2	103 ± 3	160 ± 2
σ(Z=12)	164 ± 8	143 ± 4	130 ± 5	141 ± 2	134 ± 3	124 ± 3	163 ± 2	109 ± 4	160 ± 2
σ(Z=11)	92 ± 4	80 ± 3	67 ± 3	68 ± 2	74 ± 2	68 ± 2	64 ± 2	61 ± 2	52 ± 2
σ(Z=10)	94 ± 5	86 ± 3	77 ± 4	72 ± 2	80 ± 2	73 ± 2	63 ± 2	64 ± 2	53 ± 2
σ(Z=9)	51 ± 3	45 ± 2	38 ± 2	31 ± 1	42 ± 1	41 ± 1	30 ± 2	38 ± 2	25 ± 1
σ(Z=8)	94 ± 8	93 ± 6	79 ± 4	68 ± 2	86 ± 5	80 ± 5	65 ± 2	73 ± 5	53 ± 2
σ(Z=7)	73 ± 6	71 ± 5	62 ± 3	40 ± 2	65 ± 4	64 ± 4	48 ± 1	59 ± 5	44 ± 1
σ(Z=6)	94 ± 8	104 ± 7	85 ± 4	73 ± 4	98 ± 6	91 ± 5	74 ± 2	88 ± 7	71 ± 2

Table 6. Fragment production cross sections of silicon on aluminum.

Si + Al	This work	This work	Flesch *et al.*	This work	This work	This work
E_{beam}	269	355	453	560	765	1160
σ(Z=13)	165 ± 11	154 ± 7	163 ± 8	141 ± 5	143 ± 4	126 ± 6
σ(Z=12)	192 ± 12	163 ± 7	163 ± 8	154 ± 6	150 ± 4	130 ± 6
σ(Z=11)	108 ± 7	98 ± 5	94 ± 6	84 ± 3	81 ± 2	80 ± 4
σ(Z=10)	111 ± 7	97 ± 4	97 ± 6	92 ± 4	90 ± 3	82 ± 4
σ(Z=9)	66 ± 5	53 ± 3	50 ± 4	50 ± 2	48 ± 1	50 ± 3
σ(Z=8)	119 ± 11	107 ± 9	102 ± 6	99 ± 6	96 ± 6	84 ± 7
σ(Z=7)	102 ± 10	89 ± 7	79 ± 5	81 ± 5	81 ± 5	70 ± 6
σ(Z=6)	132 ± 12	129 ± 10	112 ± 6	121 ± 8	117 ± 7	109 ± 9

Table 7. Fragment production cross sections of silicon on copper.

Si + Cu	This work	This work	Flesch *et al.*	This work	This work	This work
E_{beam}	273	344	442	545	765	1150
σ(Z=13)	211 ± 20	184 ± 9	193 ± 10	189 ± 6	193 ± 5	185 ± 7
σ(Z=12)	223 ± 20	197 ± 9	198 ± 10	192 ± 6	187 ± 5	182 ± 7
σ(Z=11)	135 ± 13	105 ± 5	100 ± 7	106 ± 3	101 ± 3	106 ± 4
σ(Z=10)	137 ± 13	113 ± 6	95 ± 7	119 ± 4	109 ± 3	107 ± 5
σ(Z=9)	70 ± 7	63 ± 3	61 ± 5	60 ± 2	62 ± 2	60 ± 3
σ(Z=8)	156 ± 18	137 ± 11	121 ± 7	126 ± 8	126 ± 8	128 ± 10
σ(Z=7)	125 ± 14	110 ± 9	90 ± 6	102 ± 6	99 ± 6	99 ± 8
σ(Z=6)	174 ± 20	153 ± 12	144 ± 8	138 ± 8	149 ± 9	142 ± 12

Table 8. Fragment production cross sections of silicon on tin.

Si + Sn	This work	This work	This work	This work	This work
E_{beam}	278	359	560	771	1155
σ(Z=13)	262 ± 27	259 ± 21	244 ± 10	258 ± 11	281 ± 14
σ(Z=12)	264 ± 27	237 ± 19	229 ± 10	221 ± 9	232 ± 12
σ(Z=11)	157 ± 17	130 ± 11	119 ± 5	118 ± 5	135 ± 8
σ(Z=10)	144 ± 16	137 ± 11	134 ± 6	129 ± 6	129 ± 8
σ(Z=9)	87 ± 10	75 ± 10	75 ± 4	72 ± 3	73 ± 5
σ(Z=8)	188 ± 23	152 ± 19	146 ± 11	153 ± 6	132 ± 12
σ(Z=7)	151 ± 19	142 ± 18	123 ± 9	119 ± 5	110 ± 11
σ(Z=6)	215 ± 26	172 ± 21	174 ± 13	188 ± 8	169 ± 17

Table 9. Fragment production cross sections of silicon on lead.

Si + Pb	This work	This work	Flesch *et al.*	This work	This work	This work
E_{beam}	274	364	430	540	770	1145
σ(Z=13)	301 ± 42	326 ± 29	362 ± 24	353 ± 10	373 ± 16	430 ± 18
σ(Z=12)	318 ± 43	254 ± 24	343 ± 22	276 ± 8	268 ± 12	314 ± 14
σ(Z=11)	189 ± 26	140 ± 16	132 ± 14	146 ± 5	143 ± 7	169 ± 9
σ(Z=10)	184 ± 26	165 ± 16	163 ± 15	157 ± 5	147 ± 7	169 ± 9
σ(Z=9)	100 ± 15	88 ± 10	70 ± 9	84 ± 3	89 ± 4	95 ± 6
σ(Z=8)	184 ± 29	161 ± 19	171 ± 15	163 ± 5	174 ± 12	158 ± 15
σ(Z=7)	187 ± 29	136 ± 19	124 ± 12	137 ± 4	148 ± 10	123 ± 13
σ(Z=6)	266 ± 40	251 ± 31	190 ± 15	220 ± 14	241 ± 17	176 ± 19

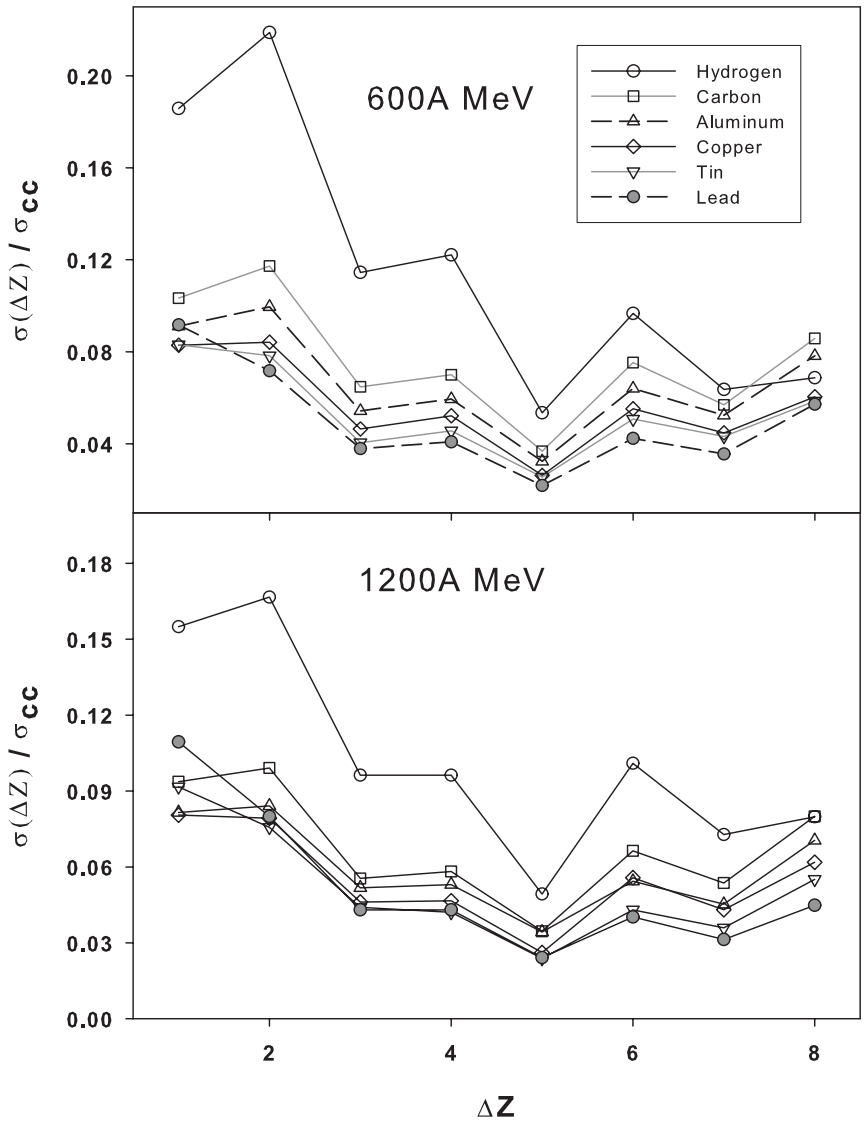

Fig. 6. For 600A MeV data (top), and 1200A MeV (bottom), the fragment cross sections divided by the charge-changing cross section, plotted as a function of charge change ΔZ.

290A MeV than at the other energies measured here. The few exceptions to this are for C targets and C (charge 6) fragments at energies below 800A MeV, and for Sn and Pb targets for Al fragments ($\Delta Z = 1$), which as noted above are likely enhanced by contributions from electromagnetic dissociation. Since the charge-changing cross sections are more or less energy-independent, and the share of the cross section going into production of fragments with charge 6 and above decreases, it must be the case that the share going into fragments of charge 5 and below increases as beam energy increases.

The energy dependence of fragment production with hydrogen targets in Fig. 7 is unlike that seen for any other material. The cross sections for charges 6 to 8 rise sharply with energy, whereas for all other targets the trend is for these cross sections to fall or stay approximately flat with energy. As noted above, the energy dependence of the charge-changing cross sections and the fragment probabilities (Fig. 6) are also distinctive for hydrogen compared to other targets. As a considerable portion of the existing fragmentation database is comprised of measurements made with H targets, it is worth noting that, based

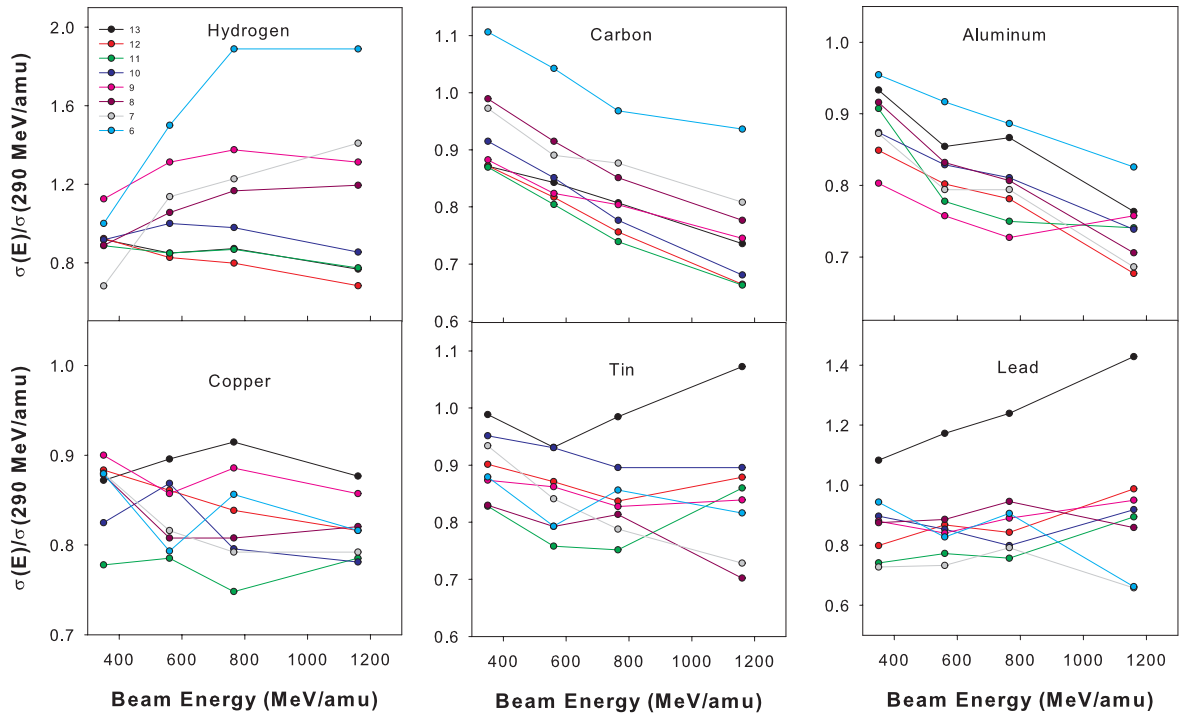

Fig. 7. Fragment cross sections divided by the cross section measured at 290A MeV. The symbol and color scheme shown in the legend at upper left applies to all graphs. The trends in the data are discussed in the text.

on the results shown here, a simple extrapolation (e.g., by scaling) of the hydrogen-target cross sections to higher-A targets would be grossly misleading.

An intriguing feature in Fig. 7 is the behavior of the Na (charge 11) cross sections. For the lightest targets, H and C, the cross section decreases with increasing energy; but as target mass increases, the data flatten at the intermediate energies (600A and 800A MeV beams) and rise at the highest energy. The Ne and Mg (charge 10 and 12) cross sections show similar, but less pronounced, changes in their energy dependence as target mass increases.

To further illustrate the trends seen in Fig. 7, we show in Fig. 8 the fragment cross sections as functions of beam energy for Al (upper plot) and Pb (lower), respectively. The data are similar to those shown in Fig. 7, but in Fig. 8 the cross sections have not been normalized to the 290A MeV data, so that the 290A MeV points can be shown, and the Flesch *et al.* data have been incorporated. (In Fig. 8, as in Fig. 7, error bars are not shown in order to keep the plots readable. However one should bear the uncertainties in mind when looking at the plots.) There is markedly different behavior for the two target materials for the charge 12 and 13 cross sections, but there are many similarities in the trends for other charges. For example, for both targets, the ordering of the cross sections is quite consistent: charge 6 is invariably the third-largest, followed by a grouping that includes (in typical order) charges 8, 10, 11, and 7, and with charge 9 having the smallest cross sections. The compatibility of the Flesch *et al.* data with ours is discussed in the following section.

5.3. *Comparison to previously-published data*

In the Al-target cross sections shown in the upper plot of Fig. 8, the Flesch *et al.* data for the most part fall in line with ours, particularly for charges 8 through 11. The agreement for charge 12 is also fairly good, but there is modest disagreement for charges 6, 7, and 13. If we interpolate between our data at 355A and 560A MeV, the Flesch *et al.* data for these charges is 1 to 2 standard deviations away from what we would expect. We note that the Flesch *et al.* point for charge 12 has been offset slightly in energy, since it would otherwise completely overlap

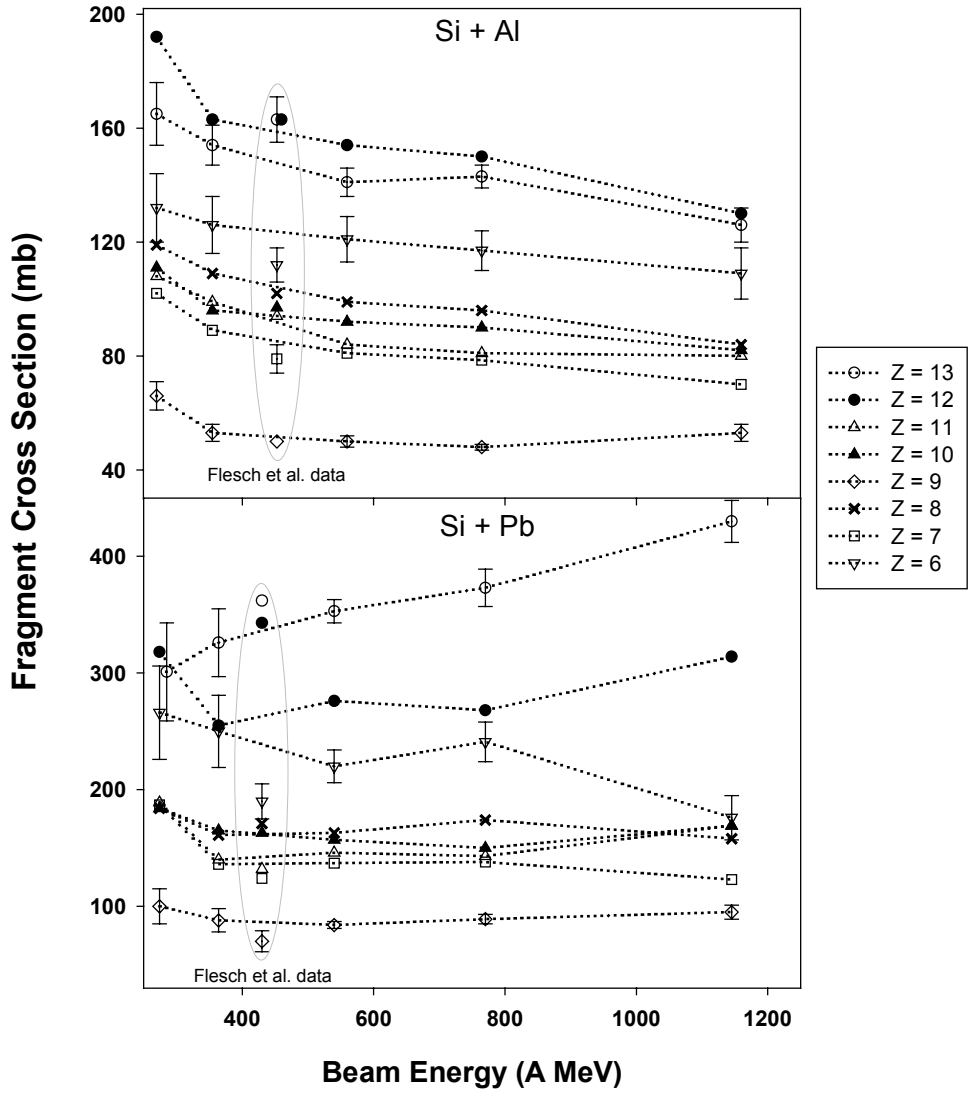

Fig. 8. Energy dependences of Al-target and Pb-target cross sections, including data from Flesch *et al.* as indicated.

the charge 13 point. [9] For clarity, only selected error bars are shown; it is possible to display the charge 6, 9, and 13 uncertainties, and also the Flesch *et al.* charge 7 point, without overly cluttering the plot.

In the Pb-target data shown in Fig. 8, the agreement with Flesch *et al.* is not as good as in the Al data. Here, charges 6 and 12 show the largest disagreements. Error bars are again shown for all charge 6, 9, and 13 data points (except Flesch *et al.* for charge 13), and our lowest-energy charge 13 data point has been offset slightly for readability. The relative errors for both experiments are largest in the Pb data, since there is comparatively little fragment production per unit target mass.

In Fig. 9, we show fragment production cross sections on hydrogen and carbon for charges 8 to 13 at all five energies reported here, alongside data from Flesch *et al.* and Webber *et al.* In Table 10, we quantify and summarize comparisons of the different experiments in those cases where beam energies were similar. In all cases but one, χ^2's per degree of freedom exceed 1.0, the approximate value one would expect to obtain if two conditions were met: 1) the fragment production cross sections are energy-independent within the narrow ranges of comparison; 2) all experimental errors are properly accounted for. The entries in Table 10 for C, Al, Cu, and Pb targets show comparatively good agreement (χ^2's less than 2 per d.o.f.) between our data and those of Flesch *et al.* For H targets, where six comparisons are possible, three cases yield χ^2's per degree of freedom between 1.7 and 2.6, indicating reasonable agreement between experiments. However, for carbon targets, agreement is reasonably good only for the comparison of our data at 560A MeV and Flesch's. The remainder of the χ^2's are large; further, the cross sections for charges 13 and 12 have opposite trends when we compare our results (cross sections decrease with energy) to those of Webber *et al.* (cross sections increase with energy), as can be seen in the plots in the upper right hand corner of Fig. 9.

We cannot identify the cause of the two very large χ^2's that are found in the comparisons of our data to Webber *et al.* for carbon at the two highest energies. The discrepancies are beyond any plausible energy dependence of the cross sections, and also beyond reasonable systematic errors. We note that χ^2 is a sensitive statistic, and the two worst cases are strongly affected by the charge 12 and 13 points. The disparities for the other fragment charges are significant, but not as large as those two.

[9] For the sake of clarity in the plot, a few other points that were fully or almost fully overlapping have been shifted, in all cases by one half of the size of the error bar, or less.

5.4. *Comparison to NUCFRG2 predictions*

Since the current standard NASA GCR transport model, HZETRN, makes use of the cross sections predicted by the NUCFRG2 code, we focus here on comparing to those predictions. NUCFRG2 is a semi-empirical cross section model based on an abrasion-ablation formulation. In the abrasion process, the region of overlap of projectile and target determines the number of nucleons removed from the projectile. The remaining spectator nucleons are in a non-spherical configuration which has excess surface energy compared to the minimum-energy sphere. This state decays (ablation) by particle emission with one nucleon emitted per 10 MeV of excitation energy. In [6], we found that NUCFRG2 reproduced ^{20}Ne fragmentation cross sections reasonably well, though it did not predict the observed enhancement of even-Z fragment cross sections. NUCFRG2 predicts this effect only for hydrogen targets, but in fact it is seen for all targets. The same effect is seen in the Si beam data presented here: the data show a clear odd-even effect that is lacking in the model. Further, NUCFRG2 does not reproduce the measured suppression of the charge 9 cross sections, nor does it accurately predict the relatively large charge 6 cross sections.

Figure 10 contains six scatterplots, one for each target element. In each plot, the cross section predicted by NUCFRG2 is plotted against the measured value, and a line is drawn at 45^o to indicate what would be a heavily-populated region if the agreement were very good. Instead, what is seen is a scatter of points to either side of the 45^o line, with few discernible trends. Only for hydrogen is there a strong suggestion of a simple offset, with the predicted cross sections tending to be smaller than the measured. We quantified these findings by calculating, for each target element/beam energy combination, the averages and standard deviations of the quantity (measured cross section/predicted cross section). The results, averaged over energy for a given target, are shown in Table 11. The standard deviations range from a low of 0.21 (H at 350A MeV) to a high of 0.51 (Pb at 364A MeV), and themselves average 0.37, indicating substantial scatter in

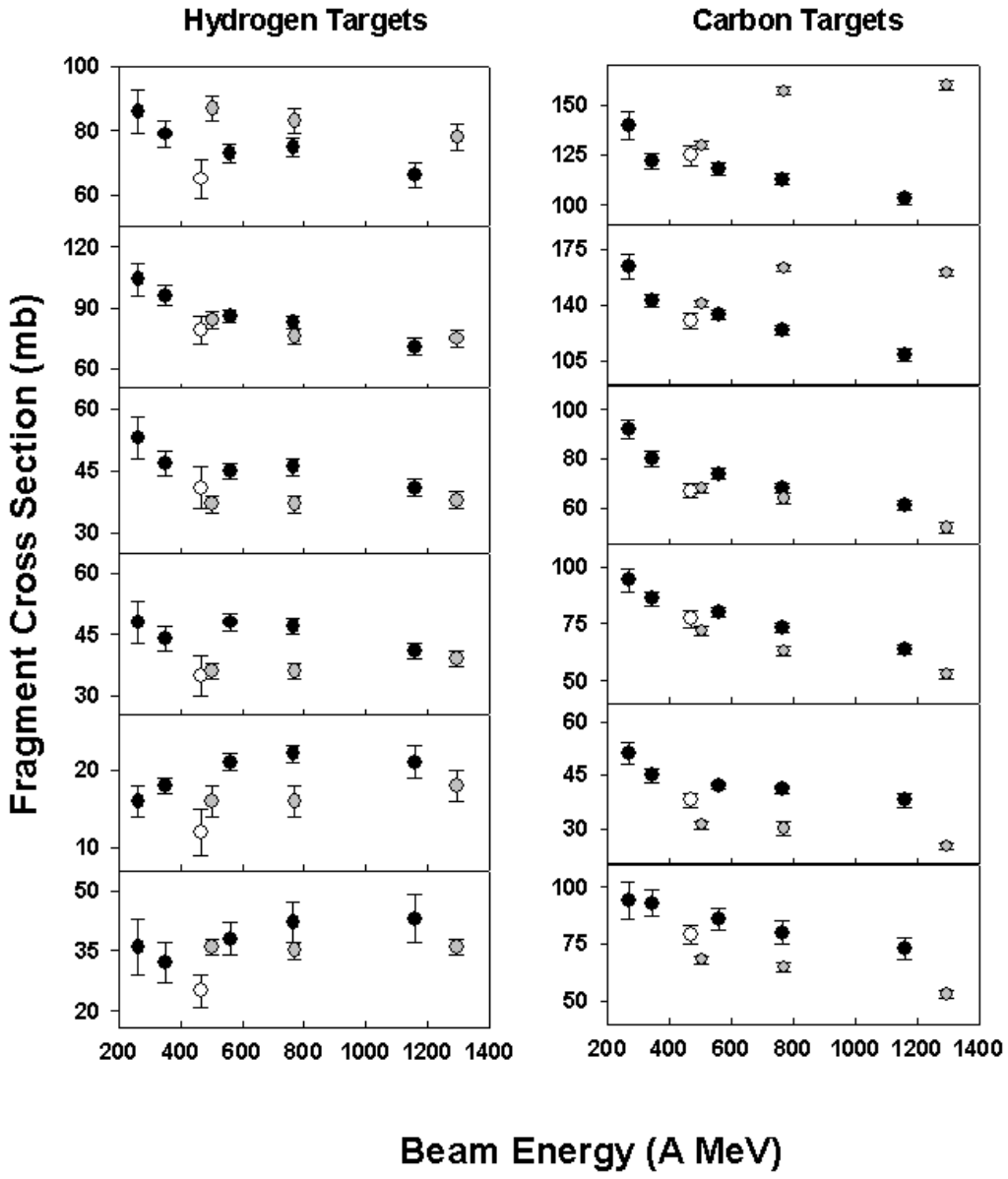

Fig. 9. From top to bottom, fragment cross sections for charges 13, 12, 11, 10, 9, and 8 for hydrogen targets (left) and carbon targets (right). Data from the present experiment are shown as solid circles; from Flesch *et al.* as open circles; and from Webber *et al.* as gray circles.

Table 10. χ^2 values for agreement of fragment production cross sections between experiments.

Target	Data Set #1	Data Set #2	χ^2 per DOF
Hydrogen	This work, E=350	Flesch *et al.*, E=467	2.5
	Flesch *et al.*, E=467	Webber *et al.*, E=503	2.6
	Webber *et al.*, E=503	This work, E=560	5.6
	This work, E=560	Flesch *et al.*, E=467	3.2
	This work, E=765	Webber *et al.*, E=770	5.7
	This work, E=1147	Webber *et al.*, E=1296	1.7
Carbon	This work, E=344	Flesch *et al.*, E=467	4.4
	Flesch *et al.*, E=467	Webber *et al.*, E=503	8.0
	Webber *et al.*, E=503	This work, E=560	15.3
	This work, E-560	Flesch *et al.*, E=467	1.6
	This work, E=765	Webber *et al.*, E=770	41.7
	This work, E=1147	Webber *et al.*, E=1296	58.4
Aluminum	This work, E=344	Flesch *et al.*, E=453	0.6
	Flesch *et al.*, E=453	This work, E=560	1.2
Copper	This work, E=344	Flesch *et al.*,E=442	1.3
	Flesch *et al.*, E=442	This work, E=545	1.6
Lead	This work, E=344	Flesch *et al.*, E=430	1.7
	Flesch *et al.*, E=430	This work, E=540	1.9

the comparisons. The standard deviations increase as target mass increases; the means are close to 1 for C and Al, but from there increase with target mass.

There are several free parameters in NUCFRG2 which have been adjusted to fit earlier published data, including those of Webber *et al.* Thus it is possible that some of the disagreement observed in the comparisons above is simply a reflection of the disagreement between our data and those of Webber *et al.* It also seems likely that the model has been tuned to the low-A range of target masses, where most of the previously reported data are.

In the context of radiation risks in spaceflight, the fairly large discrepancies we find may be acceptable, given the other large uncertainties in the problem, which are dominated by a lack of understanding of biological response to heavy ions. However, in the context of model development, these discrepancies suggest there is still considerable room for improvement.

6. Conclusions

We have measured charge-changing and fragment production cross sections for ^{28}Si beams with extracted energies between 290A and 1200A MeV. The results have been compared to earlier measurements at similar energies and to the NUCFRG2 model. Charge-changing cross sections reported here for C, Al, Cu, Sn, and Pb targets show no significant energy dependence over the 270A to 1150A MeV range of target-center energies. The H-target charge-changing cross section increases slightly as energy increases, a trend also seen in the Webber *et al.* data. The effect is weak, slightly beyond the one-sigma experimental uncertainties. The charge-changing cross sections reported here agree reasonably well with the earlier experiments, and with NUCFRG2, typically at the 2% to 4% level.

Fragment production cross sections in the range from $Z_f = 6$ to 13 have been extracted. For C and Al targets, fragment cross section decrease with increasing energy. Contributions to the $\Delta Z = 1$ from electromagnetic dissociation are apparently seen with Pb and Sn targets, and appear to be energy dependent. As reported in previous measurements of fragmentation cross sections of ^{56}Fe and ^{20}Ne beams, the production of even-Z fragment species is favored at all energies. Production of fluorine, $Z_f = 9$, is noticeably suppressed for all targets. The cross

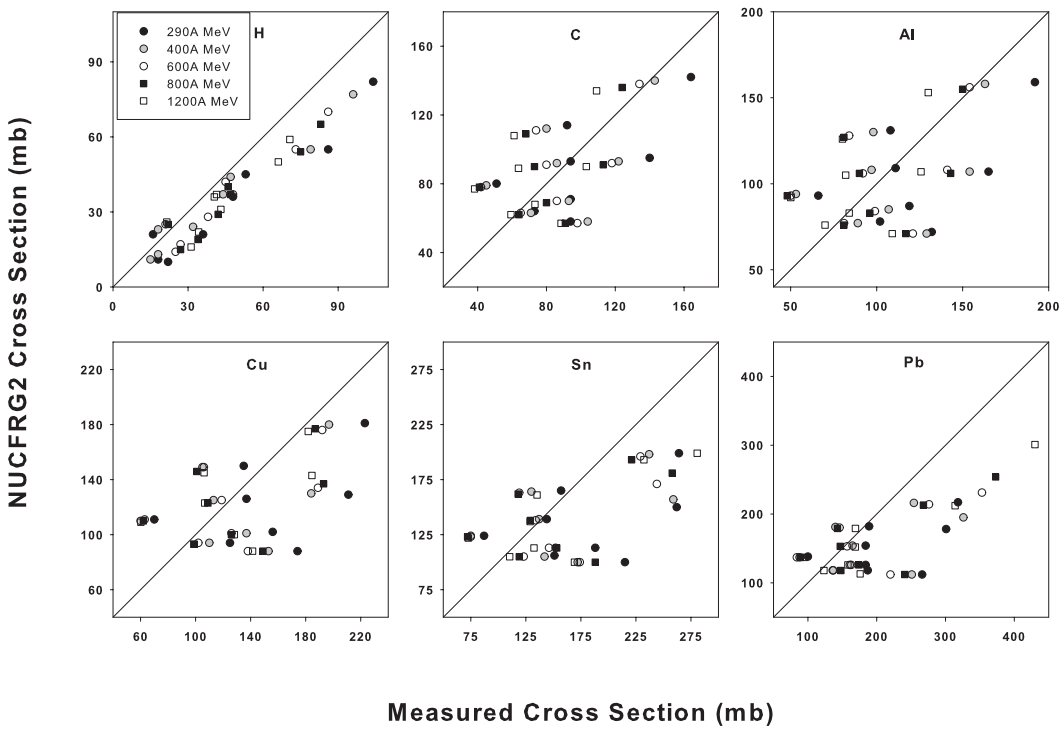

Fig. 10. Scatterplots of fragment cross sections for charges 6 to 13 predicted by the NUCFRG2 model (vertical axis) vs. measured cross sections (horizontal axis). Cross sections are grouped by target; the symbol types indicate the beam energy.

Table 11. Ratios of the measured fragment cross sections to predicted cross sections using the NUCFRG2 model.

Target (Measured σ/NUCFRG2 σ)	Std. Deviation of Ratios	
H	1.336	.316
C	1.038	.356
Al	1.067	.365
Cu	1.210	.364
Sn	1.288	.386
Pb	1.363	.408

sections for production of lighter fragments, $Z_f < 6$, increase as beam energy increases, consistent with the simple notion that, with increasing kinetic energy available in the collision, there is a higher probability for additional nucleons to be removed from the projectile due to greater excitation of the prefragment and/or greater energy transfer in the collision for a given impact parameter. Presumably a similar trend exists in the breakup of the target nuclei as well, but that cannot be assessed in these data since we measure only the projectile fragments. The measured fragment cross sections agree fairly well with previous data for hydrogen targets and for aluminum, copper, and lead; however, significant disparities exist among the different measurements using carbon targets, particularly for charges 12 and 13 in the range from 765A to 1296A MeV. There are also significant disparities when comparing to the NUCFRG2 model, with differences between the data and model typically on the order of 30%.

7. Acknowledgements

We gratefully acknowledge the efforts of the accelerator operators at both HIMAC and the Brookhaven AGS to provide us with excellent beams and stable conditions in these experiments. We particularly wish to thank Dr. E. Takada of HIMAC for his superb work in supervising the beam delivery. This work was supported at LBNL by the Space Radiation Health Program of the National Aeronautics and Space Administration under NASA Grant Numbers L14230C, H31909D, and H34854D, through the U.S. Department of Energy under Contract No. DE-AC02-05CH11231. At HIMAC, this work was supported in part by the Research Project with Heavy Ions at NIRS-HIMAC, Project Number P037. Three of us (S.G, L.H., and J.M.) acknowledge, with much gratitude, the travel support we have received from the Japan Society for the Promotion of Science (JSPS).

8. Appendix – Beamline Configurations

At HIMAC, where most of the measurements were performed, the beam spot is small, typically with a FWHM of a few millimeters in both x and y (the dimensions transverse to the beam axis). The low intensities needed to avoid damaging these silicon detectors (about 10^3 particles cm^{-2} sec^{-1}) are easily achieved, and the spills tend to be uniform over about 0.6 sec; the result is that little event pile-up is seen in the data. Because the beam spot is small, there is no need to have a large detector upstream of the target to veto events with multiple incident beam ions, and a trigger detector with a radius of 0.4 cm is adequate. In the 1998 experiment the second detector upstream of the target was 5 mm thick with a radius of 2 cm; in 1999, 2002, and 2003, the second detector was 3 mm thick with an active radius of 1.1 cm. In all HIMAC experiments, time-of-flight measurements were performed using two thin plastic scintillation counters. A 12.7 cm thick NaI counter was placed downstream of the second plastic scintillator. The depth of NaI was sufficient to stop the primary ions and some secondaries; this allows isotopic identification of fragments in a small number of cases. The scintillators are placed downstream of the last silicon detector.

At the AGS, the beamline was optimized for radiobiology experiments, with a large spot (7 cm diameter) and comparatively high intensity (typically on the order of 10^6 particles cm^{-2} sec^{-1}). Tuning for the low intensity required for successful running of silicon detectors – about three orders of magnitude lower than for radiobiology – is difficult since the beam monitoring hardware was optimized for much higher intensities. Experience has shown that with a large beam spot, it is best to use a trigger detector with a radius comparable to that of the particle identifier detectors that are placed downstream of the target, and it is also important to place one or more relatively large detectors upstream of the target in order to reject (off-line) events with multiple beam ions incident on the target. When a small trigger detector is used with a large beam spot, a large fraction of events must be rejected in the off-line analysis due to the presence of a second particle in the large-area detectors downstream of the target. Accordingly, for the data obtained at the AGS, we used a trigger detector with a radius of 1.2 cm and placed a pair of position-sensitive detectors (radius 22 mm) upstream of the target position to allow

identification of events in which a second beam ion was present during the 10 μsec ADC gating time.

References

[1] F.A. Cucinotta, W. Schimmerling, J.W. Wilson, L.E. Peterson, G.D. Badhwar, P.B. Saganti, and J.F. Dicello, Radiat. Res. 156 (2001) 682.

[2] J.A. Simpson, in Composition and Origin of Cosmic Rays, edited by M. M. Shapiro (Reidel, Dordrect, 1983), 1.

[3] G.D. Badhwar and P.M. O'Neill, Nuclear Tracks and Radiation Measurements 20 (1992) 403.

[4] J.W. Wilson, F.F. Badavi, F.A. Cucinotta, J.L. Shinn, G.D. Badhwar, R. Silberberg, C.H. Tsao, L.W. Townsend, and R.K. Tripathi (1995) NASA TP 3495.

[5] C. Zeitlin, L. Heilbronn, J. Miller, S. E. Rademacher, T. Borak, T. R. Carter, K. A. Frankel, W. Schimmerling, and C. E. Stronach, Phys. Rev. C56 (1997) 388.

[6] C. Zeitlin, A. Fukumura, L. Heilbronn, Y. Iwata, J. Miller, T. Murakami, Phys. Rev. C (2001) 64:024902

[7] National Council on Radiation Protection and Measurements, Guidance on Radiation Received in Space Activities, NCRP Report No. 98 (1989) 22.

[8] H.C. Bradt and B. Peters, Phys. Rev. 77 (1950) 54.

[9] A.S. Goldhaber, Phys. Lett. 53B (1974) 306.

[10] R.K. Tripathi and L.W. Townsend, Phys. Rev. C49 (1994) 2237.

[11] C. Zeitlin, L. Heilbronn, J. Miller, W. Schimmerling, L.W. Townsend, R.K. Tripathi, J.W. Wilson, Radiat. Res. 145 (1995) 666.

[12] F. Flesch, G. Iancu, W. Heinrich, and H. Yasuda, Radiat. Meas. 34 (2001) 237.

[13] W.R. Webber, J.C. Kish and D.A. Schrier, Phys. Rev. C41 (1990) 533.

[14] J.W. Wilson, J.L. Shinn, L.W. Townsend, R.K. Tripathi, F.F. Badavi, and S.Y. Chun, Nucl. Instr. Meth. B94 (1994) 95.

[15] H.H. Heckman and P.J. Lindstrom, Phys. Rev. Lett. 37 (1976) 56.